

**3-D EULER AND NAVIER-STOKES CALCULATIONS  
FOR AIRCRAFT COMPONENTS**

Veer N. Vatsa

NASA Langley Research Center, Hampton, Virginia

Bruce W. Wedan

Vigyan Research Associates, Hampton, Virginia

Eli Turkel

ICASE, Hampton, Virginia

**Abstract**

An explicit multistage Runge-Kutta type of time-stepping scheme is used for solving transonic flow past a transport type wing/fuselage configuration. Solutions for both Euler and Navier-Stokes equations are obtained for quantitative assessment of boundary-layer interaction effects. The viscous solutions are obtained on both a medium resolution grid of approximately 270,000 points and a fine grid of 460,000 points to assess the effects of grid density on the solution. Computed pressure distributions are compared with the experimental data.

**Introduction**

The availability of present generation supercomputers has made it feasible to compute transonic flow over realistic aircraft components, which is evident from the multitudes of papers that have appeared in the literature on this subject in the last 3-4 years. Euler solutions for essentially complete aircraft configurations [1-2] are now available. In addition, Navier-Stokes solutions for aircraft components, such as wings, fuselage-shaped bodies and simple configurations [3-8] have also become available recently. Another problem that has received special attention recently is that of flow over a simple aircraft component, such as a wing, mounted inside a wind tunnel [9-12]. Navier-Stokes solutions for such problems, including simulation of tunnel walls and sting support, are very useful for estimating wind tunnel wall-interference effects.

In the present paper, a multistage Runge-Kutta type of time-stepping scheme developed by Jameson and coworkers [13-14] for Euler equations, and extended to three-dimensional Navier-Stokes equations by Vatsa [5], is applied to the computation of a transport -type wing/fuselage configuration under transonic flow conditions. The accuracy of this numerical scheme has been tested extensively for high Reynolds number viscous flow over simple components such as prolate spheroids and wings in free-air and inside wind tunnels [5,8,12]. In this paper, the numerical scheme of Ref. 5 is extended to solve the flow over a wing/fuselage configuration.

**Governing equations and numerical algorithm**

The basic equations describing the general three-dimensional flow are the compressible Navier-Stokes equations. These are written in a body-fitted curvilinear coordinate system ( $\xi$ ,  $\eta$ ,  $\zeta$ ), where  $\xi$ ,  $\eta$ , and  $\zeta$  represent the streamwise, normal and spanwise directions

respectively. Since the dominant viscous effects for high Reynolds number flow are confined to a thin viscous layer near the body surface, a thin-layer assumption is employed here by retaining only the viscous diffusion terms along the  $\eta$ -direction, which is normal to the surface. These equations can be written in the conservation law form as :

$$\frac{\partial(J^{-1}U)}{\partial t} + \frac{\partial F}{\partial \xi} + \frac{\partial G}{\partial \eta} + \frac{\partial H}{\partial \zeta} = \frac{\partial G_v}{\partial \eta} \quad (1)$$

where  $U = [\rho, \rho u, \rho v, \rho w, \rho E]^T$

represents the dependent variables; F, G and H represent the convective fluxes and  $G_v$  represents the viscous fluxes. The full form of these terms is readily available in the literature (e.g. see Refs. 3,7,12).

The concepts of eddy viscosity and eddy conductivity are employed to account for the effect of turbulence. The Baldwin-Lomax turbulence model, which is an algebraic model, is used for the present turbulent flow calculations.

A finite-volume algorithm based on Jameson's Runge-Kutta time-stepping scheme is used for obtaining steady-state solutions to the governing equations. The spatial derivatives are replaced with central differences and the solution is advanced in time using a 4-stage Runge-Kutta scheme. Local time-stepping, enthalpy damping and implicit residual averaging techniques are used for accelerating the convergence to steady state.

### Artificial dissipation

A blend of second and fourth order artificial dissipation is added to the central-difference scheme for suppressing odd-even point decoupling and oscillations in the vicinity of shock waves and stagnation points. The dissipation model used here is based on the model devised by Jameson and Baker [14] for 3-D Euler equations. Whereas the dissipation model of Ref. 14 works reasonably well for Euler equations on grids with cell aspect ratios of order one, the situation is less satisfactory when seeking solutions to Navier-Stokes equations. This is due to the fact that extremely fine meshes with large stretchings have to be used for accurate resolution of the thin boundary-layer regions that develop at high Reynolds number. This gives rise to high aspect ratio cells and the dissipation model of Ref. 14 results in excessive levels of artificial dissipation under these conditions.

Martinelli [15] and Swanson and Turkel [16] have looked at different ways of reducing the artificial dissipation in 2-D Navier-Stokes computations. Vatsa, Thomas and Wedan [8], and Vatsa and Wedan [12] have studied the effects of artificial dissipation on the accuracy of 3-D Navier-Stokes solutions for transonic flow over prolate spheroids and wings. Based on these studies [8,12,15,16], it was concluded that an effective way to reduce the artificial dissipation levels is to scale the dissipation in the three coordinate directions by their respective eigenvalues instead of scaling the dissipation by the maximum eigenvalue, as was done in the original work of Ref. 14. In addition, the artificial dissipation is scaled with the local Mach number to reduce it even further in the viscous layer. Based on the earlier investigations [8,12], this modified dissipation model provides improved level of accuracy for the solutions of the Navier-Stokes equations, and hence it will be employed in the present paper.

### Boundary conditions

The wing/fuselage surface is treated as a solid, no-slip and no-injection boundary. Numerically, this boundary condition is imposed by setting the three velocity components,  $u$ ,

$v$  and  $w$  to zero at the surface. The normal pressure and temperature gradients at this surface are set to zero. Only one-half of the wing/fuselage configuration (left-half) is simulated and hence a symmetry condition in the spanwise direction is imposed at  $\zeta = 0$  for all variables except the cross-flow velocity component,  $w$ , which is taken to be antisymmetric. The farfield boundary condition is based on Riemann invariants for one-dimensional flow normal to the boundary, as discussed by Jameson and Baker [14] and Thomas and Salas [17]. Extrapolation on all variables is used at the downstream boundary.

### Grid generation

A transfinite interpolation scheme based on Eriksson's [18] methodology is used for generating the three-dimensional grids for the wing/fuselage configuration under consideration here. A C-O grid topology is employed for accurate resolution of the wing leading-edge and wing-tip regions. Grid clustering is used to provide good resolution in regions of large flow gradients. A partial view of the grid is shown in Fig. 1. As can be seen from this figure, the grid generation code employed here can be used to generate reasonable grids for wing/fuselage configurations. The main deficiencies in this grid topology are the lack of resolution in the fuselage nose region and significant skewness in the wing-root and wing-tip regions, which may be relieved through the concepts of block-structured grids.

### Results and discussion

In this paper, we will concentrate on calculations for a transport-type wing/body configuration, specifically the Pathfinder I [19]. Experimental pressures for this configuration were obtained in the NTF wind tunnel at NASA Langley, Virginia. The test conditions for the case considered here are  $M_\infty = 0.801$ ,  $\alpha = 1.998^0$  and a Reynolds number of 3 million. Transition of the flow to turbulence was taken to be at 10% of the chord on the wing, and at the fuselage nose for all the calculations presented here. The position of transition corresponds to the experimental placement of transition strips for the wing.

The present computations were made for a mid-mounted wing configuration, while the configuration tested had a low-mounted wing. This was done mainly to obtain solutions within the time constraint required by this symposium, since the surface definition of the mid-mounted wing configuration was readily available from an earlier investigation [20]. It is not known what total effect this may have had on the present solutions, however based on the interacting boundary layer calculations of Ref. 20, the effect on the solution from the wing position should be apparent only in the vicinity of the wing/fuselage juncture. It is planned to repeat the present Navier-Stokes computations in near future for the low-mounted wing configuration to simulate the experimental set up more precisely. It should also be pointed out that the calculations performed here used nominal wing coordinates obtained from spanwise linear interpolation of a limited amount of data describing the wing. As a result the computational model of the wing contained some localized curvature discontinuities which resulted in pressure oscillations in the solution. These oscillations are small, however, and the overall solution was not affected.

The first set of calculations to be presented are for a medium resolution grid of  $161 \times 41 \times 41$  points in the streamwise, spanwise and normal directions, respectively. The normal spacing of the grid was  $4 \times 10^{-5}$  at the wing and fuselage surface, giving a  $y^+$  value of approximately 5 for the viscous calculations. Of the 40 cells in the spanwise direction, 16 of these were placed on the fuselage. Both viscous and inviscid calculations were performed on this grid. Fig. 2 shows the convergence history for the viscous calculations on this grid in terms of orders of reduction in the average residual and the number of supersonic points non-

dimensionalized by the final value. This is typical for the calculations presented in this paper in that generally 5 orders of reduction were obtained for the average residual in about 2000 iterations.

The computed pressures are compared with the experimental data at 4 span stations in Fig. 3. The first span station ( $\eta = 0.131$ ) is shown only to indicate the effect of the mid-mounted wing as opposed to the low wing. As seen in this figure, the mid-fuselage mounting of the wing provides flow relief on both the upper and lower surfaces, and thus the acceleration of the flow is not as great as for the experiment. This is particularly evident on the upper surface of the wing where, with the low-wing configuration, there is actually contraction of the stream-tube in the juncture region due to the outward bulge of the fuselage above the wing. As is apparent at the next span station, this problem is reduced away from the juncture region.

Comparing the inviscid and viscous solutions in Fig. 3, it can be seen that the overall effect of including the boundary layer is to increase the pressure on the upper surface of the wing, bringing it more in line with the experimental values. In addition, there is a decrease in the computed pressure in the trailing edge region on the lower surface of the wing due to a filling in of the cove. Some oscillations in the pressure are apparent at the inboard stations for the viscous calculations, which are the result of the non-smooth geometry discussed previously. These oscillations are not seen in the inviscid calculations, however, which is attributed to much higher levels of artificial dissipation resulting from the dissipation model employed for the inviscid calculations (see Ref. 14). The major deficiency in these calculations is the lack of resolution of the leading edge acceleration and shock position and strength. In an earlier paper, Vatsa and Wedan [12] have shown that inadequate grid resolution in either the streamwise or spanwise directions will result in similar disagreements, thus the calculations were repeated for this case on a finer grid.

The next set of calculations are for a finer grid consisting of  $193 \times 49 \times 49$  points. Again, 16 of the spanwise cells were placed on the fuselage. The net increase in resolution on the wing surface was approximately 70%. The normal spacing off the surface and farfield boundaries were kept nearly the same, thus the additional 8 cells in the normal direction had the effect of reducing the stretching rate of the grid, and thus the magnitude of the added artificial dissipation. The pressure comparisons with experiment are shown in Fig. 4 for an inboard, mid-span, and an outboard span station. At the mid-span section, the finer grid improves the agreement between the calculations and the experiment in that the leading edge pressure peak and shock position and strength are better resolved. There is no significant difference between the two calculations at the inboard station, however. Both calculations miss the acceleration in the leading edge region and the shock. It is possible that the disagreement between the computed and experimental pressures at this station is due to the wing mounting position. Experimentally, the flow in the leading edge region of the wing is supersonic from the wing root/fuselage juncture to the tip, with a well developed shock structure. For the calculations, however, the flow is subsonic at the wing root, thus the shock which forms over the mid and outboard regions of the wing must vanish as the root juncture region is approached. This discrepancy will be resolved in future calculations, where the wing will be properly located on the fuselage for more accurate representation of the experimental geometry. A different situation exists at the outboard station, in that the finer grid calculation overpredicts the leading edge pressure peak and indicates a shock that is further downstream and stronger than the experimental data. This is attributed to a certain amount of experimentally observed washout of the tip due to aerodynamic loads during testing. An attempt will also be made to ascertain the magnitude of this, and include it in future calculations.

Surface streamline plots from the calculations are shown in Fig. 5 for the upper and lower surfaces of the wing. As can be seen in this figure, the flow is well behaved over the entire wing under these conditions, aside from the small streamwise extent of trailing edge separation on the upper surface. A significant amount of spanwise flow can also be observed on the lower surface in the cove region of the wing. Although, no experimental oil flows were

taken for this test, these patterns have been compared with oil flow photographs obtained for a similar configuration in another wind tunnel [21]. The streamline patterns from the calculations have qualitatively the same nature as indicated in those oil flows.

The streamline patterns for the fuselage as obtained from the calculations are also shown in Fig.5 . Again, no experimental verification of this pattern is available for this configuration. The streamline patterns, however, compare favorably with those observed previously by Vatsa and Wedan for calculations of a wing mounted on a side wall in a wind tunnel [12]. The streamline patterns from both calculations show the displacement of the streamlines away from the wing surface both above and below the wing, and a plume-type structure emanating from the wing trailing edge and extending downstream.

## Conclusions

Viscous and inviscid flow calculations have been performed for a transport-type wing/body configuration and compared to experimental data at Mach number of 0.801, an angle of attack of 1.998 degrees, and a chord Reynolds number of 3 million. The viscous calculations showed significant improvement over the inviscid calculations, particularly over the upper surface of the wing and in the cove region on the lower surface. The upper surface shock and the flow in the leading edge region were resolved more accurately on the finer grid over the mid and outboard sections of the wing. Significant differences exist between the computed and experimental pressures over the inboard region of the wing. This has been attributed to the mid-wing modeling of the configuration in the computations as opposed to the actual low-wing experimental configuration. These calculations will be repeated in the near future for a low-mounted wing configuration in order to obtain more accurate simulation of the experimental setup. Finally, the streamline patterns on the wing and fuselage compare qualitatively with patterns observed from previous computations and experimental tests of similar configurations.

## References

1. Jameson, A., Baker, T.J. and Weatherill, N.P., "Calculation of Inviscid Transonic Flow Over a Complete Aircraft", AIAA Paper 86-0103, Jan. 1986.
2. Sawada, K. and Takanashi, S., "A Numerical Investigation on Wing/Nacelle Interferences of USB Configurations", AIAA Paper 87-0455, Jan. 1987.
3. Fujii, K., and Obayashi, S., "Navier-Stokes Simulations of Transonic Flows over a Wing-Fuselage Combination", AIAA J., Vol. 25, Dec. 1987, pp.1587-1596.
4. Thomas, J.L., Taylor, S.L. and Anderson, W.K., "Navier-Stokes Computations of Vortical Flows Over Low Aspect Ratio Wings", AIAA Paper 87-0207, Jan. 1987.
5. Vatsa, V.N., "Accurate Numerical Solutions for Transonic Viscous Flow Over Finite Wings", Journal of Aircraft, Vol. 24, June 1987, pp.377-385.
6. Holst, T.L., Gundy, K.L., Flores, J. and Chaderjian, N.M., "Numerical Solution of Transonic Wing Flows Using an Euler/Navier-Stokes Zonal Approach", AIAA Paper 85-1640, July 1987.

7. Agarwal, R.K., Underwood, R.R. and Deese, J.E., "Computation of Three-Dimensional Transonic Viscous Flowfields Using Unsteady Parabolized Navier-Stokes Equations", AIAA Paper 85-1595, July 1985.
8. Vatsa, V.N., Thomas, J.L. and Wedan, B.W., "Navier-Stokes Computations of Prolate Spheroids at Angle of Attack", AIAA Paper 87-2627-CP, Aug. 1987.
9. Obayashi, S., Fujii, K. and Gavali, S., "Navier-Stokes Simulation of Wind-Tunnel Flow Using LU-ADI Factorization Algorithm", NASA TM 100042, Feb. 1988.
10. Chaderjian, N.M., "Navier-Stokes Simulation of Transonic Wing Flowfields Using a Zonal Grid Approach", NASA TM 100039, Jan. 1988.
11. Kaynak, U. and Flores, J., "Advances in the Computation of Transonic Separated Flows Over Finite Wings", AIAA Paper 87-1195, June 1987.
12. Vatsa, V.N. and Wedan, B.W., "Navier-Stokes Solutions for Transonic Flow Over a Wing Mounted in a Tunnel", AIAA Paper 88-0102, Jan. 1988.
13. Jameson, A., Schmidt, W. and Turkel, E., "Numerical Solutions of the Euler Equations by Finite Volume Methods Using Runge-Kutta Time-Stepping Schemes," AIAA Paper 81-1259, 1981.
14. Jameson, A. and Baker, T.J., "Solution of the Euler Equations for Complex Configurations", AIAA Paper 83-1929, July 1983.
15. Martinelli, L., "Calculation of Viscous Flows with Multigrid Methods", Ph.D. Dissertation, MAE Department, Princeton University, 1987.
16. Swanson, R.C. and Turkel, E., "Artificial Dissipation and Central Difference Schemes for the Euler and Navier-Stokes Equations", AIAA Paper 87-1107, June 1987.
17. Thomas, J.L. and Salas, M.D., "Far-Field Boundary Conditions for Transonic Lifting Solutions to the Euler Equations", AIAA Paper 85-20, Jan. 1985.
18. Eriksson, L.E., "Transfinite Mesh Generation and Computer Aided Analysis of Mesh Effects", Ph.D. Thesis, Uppsala University, Sweden, March 1984.
19. Young, C.P., Jr., "Pathfinder Model Program for the National Transonic Facility", NASA CP 2183, 1980, pp. 37-52.
20. Melson, N.D., "Three-Dimensional Transonic Viscous Inviscid Interaction Program", NASA TM 89037, 1986, pp. 3.
21. Bartlett, D.W. , "Wind-Tunnel Investigation of Several High Aspect Ratio Supercritical Wing Configurations on a Wide Body Type Fuselage", NASA TMX 71996, July 1977.

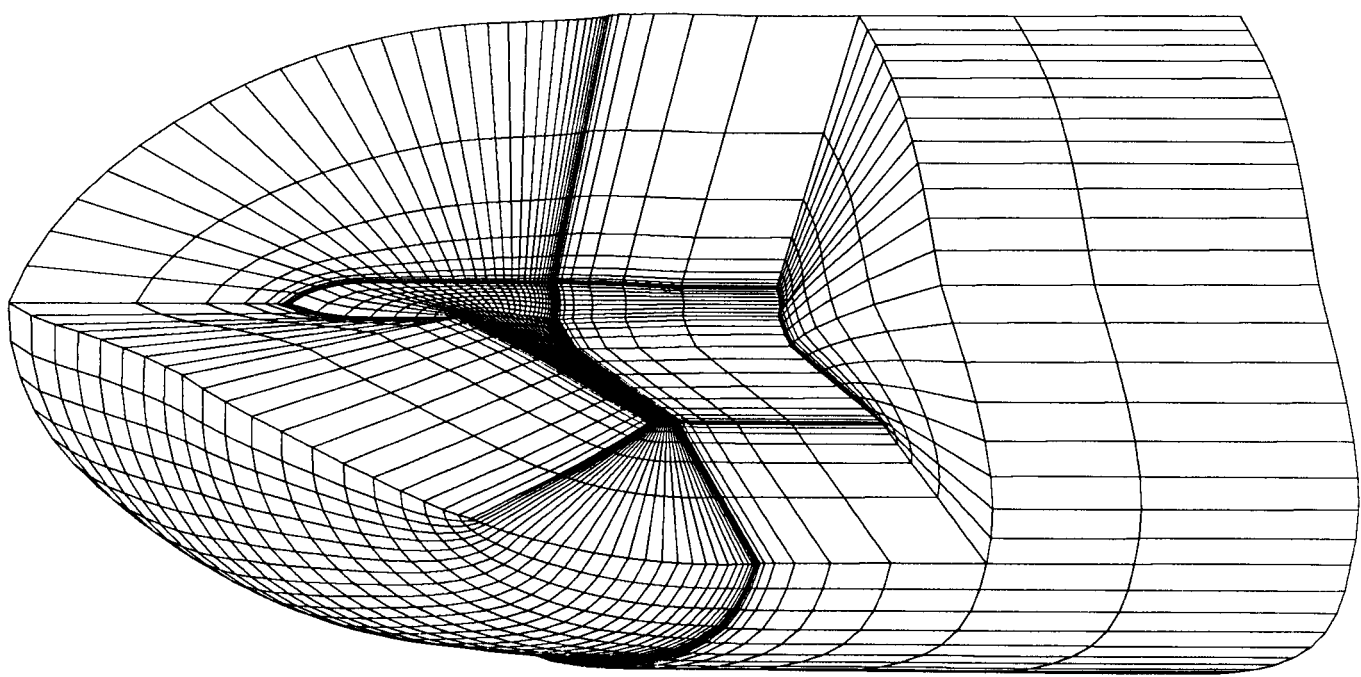


Fig.1 Partial view of Pathfinder wing/fuselage grid

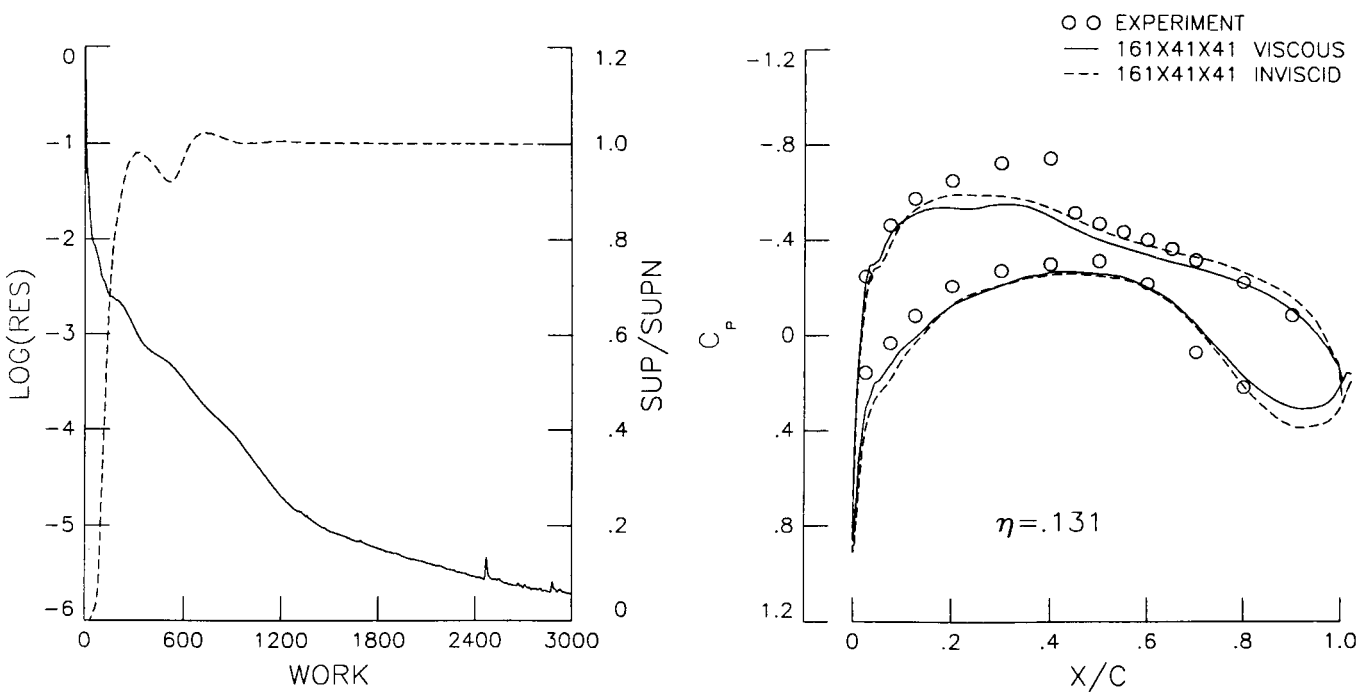


Fig.2 Convergence history for Navier-Stokes calculations on 161x41x41 grid

Fig.3 Viscous and inviscid pressure comparisons on 161x41x41 grid with experimental data

(cont.)

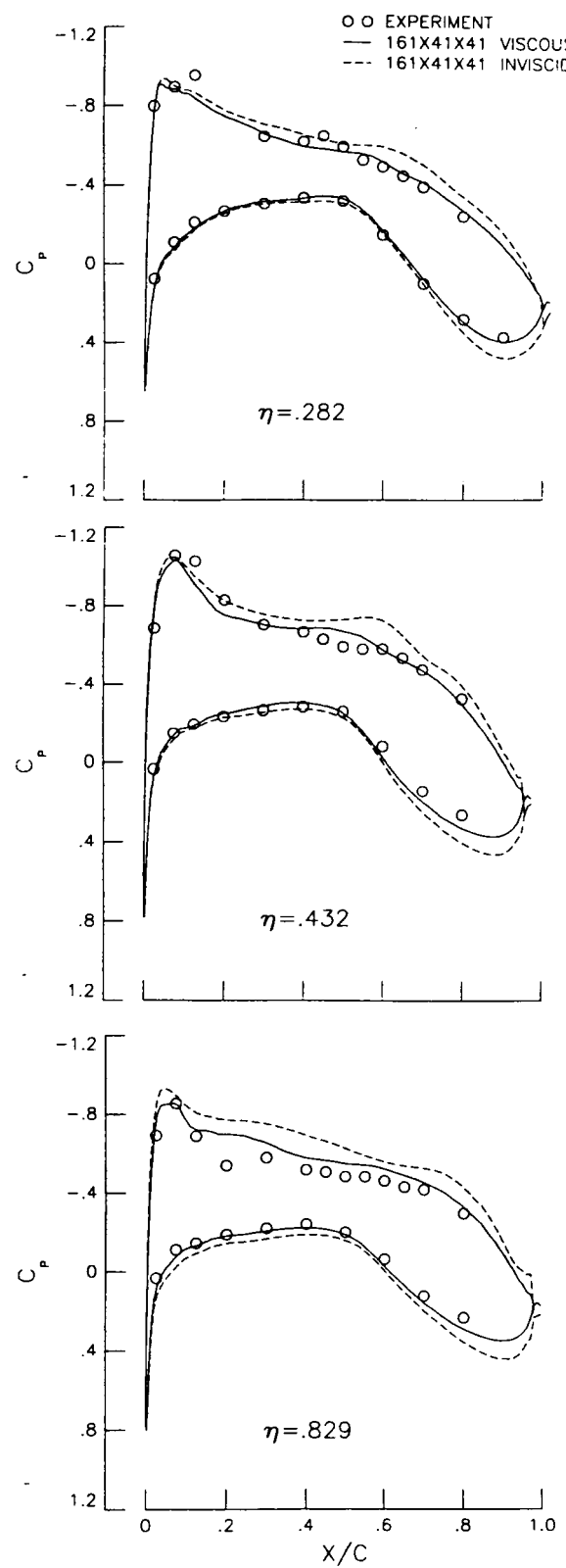


Fig.3 Viscous and inviscid pressure comparisons on 161x41x41 grid with experimental data  
 (concluded)

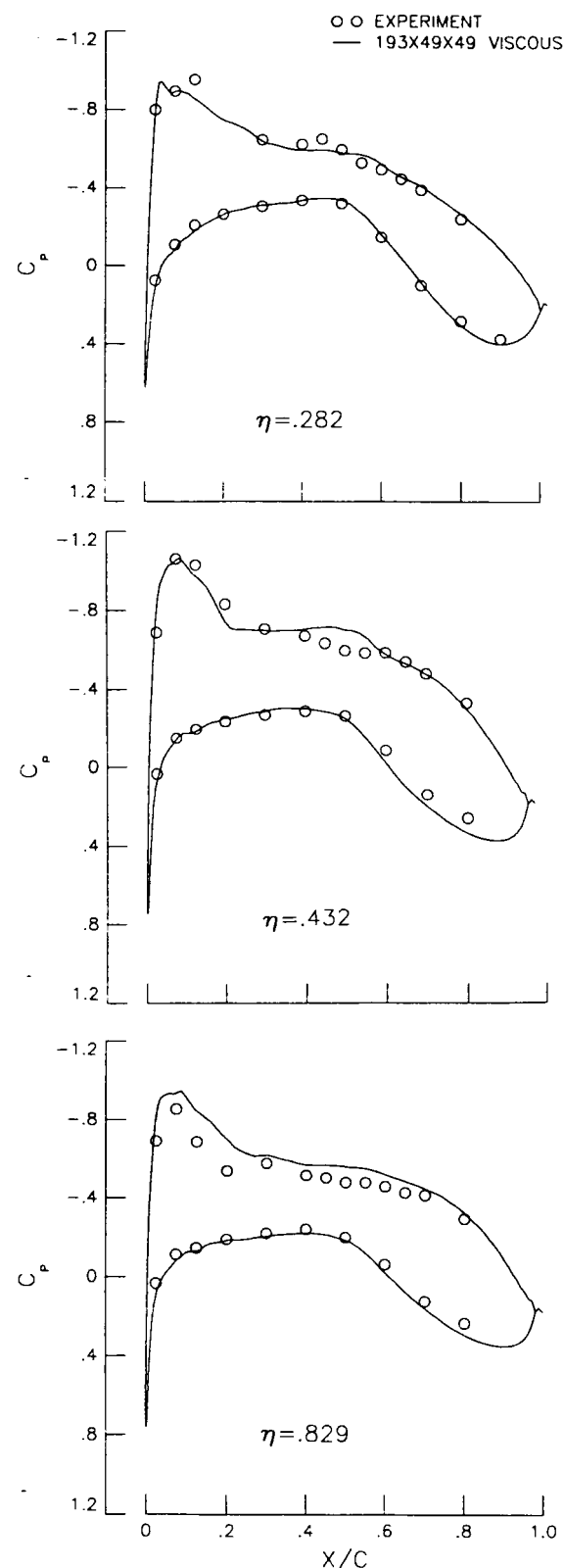


Fig.4 Comparision of viscous pressure distributions on 193x49x49 grid with experimental data

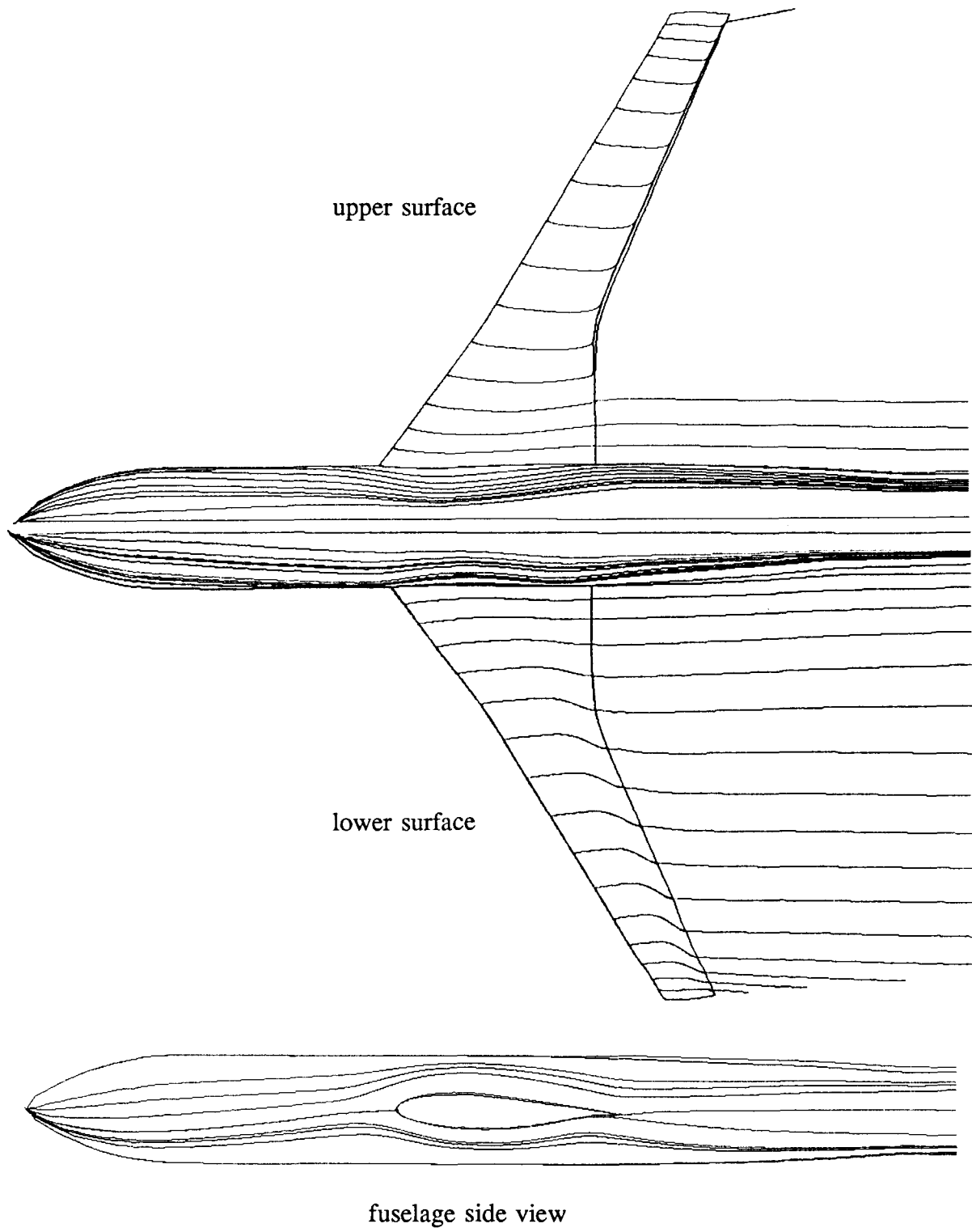


Fig.5 Surface streamline patterns on Pathfinder wing/fuselage configuration